VIII ECCOMAS Thematic Conference on Smart Structures and Materials
SMART 2017
A. Güemes, A. Benjeddou, J. Rodellar and Jinsong Leng (Eds)

3D DESIGN OF A LARGE-DISPLACEMENT DROOP-NOSE WING DEVICE

SRINIVAS VASISTA* **AND HANS PETER MONNER***

* Institute of Composite Structures and Adaptive Systems
German Aerospace Center (DLR)
Lilienthalplatz 7, 38108, Braunschweig, Germany
E-mail: srinivas.vasista@dlr.de, www.dlr.de/fa/en

Key words: Morphing Wing, Droop-nose, High-lift, Structural Optimization.

Abstract. The 3D structural design of a morphing droop-nose device for a new high-lift system is presented in this paper. This new type of high-lift system is anticipated to reduce airframe noise, takeoff and landing speeds and thus runway length, and be capable of actively producing a range of lift coefficients as per demand. A structural design process using optimization tools was further developed and applied to the case of large target deflections required for this high-lift system. The results of the 3D optimization of thickness distribution, stringer position, and force introduction points on a hybrid fiberglass-elastomeric composite skin showed close agreement to the target shapes under different aerodynamic load cases. The design of a kinematic system of linkages was also performed and upon input actuation the outer surface conformed to the target aerodynamic shapes. Required actuator torque in this design was shown to be high in the order of 3600 Nm thought actuators are available which meet the internal space requirements. Reported strains were within design limits in the order of 1.5%. The design is set to be refined in the near future with manufacturing and ground tests to follow.

1 INTRODUCTION

A large-displacement morphing wing droop-nose device with smooth shape variation is a mandatory component of the novel high-lift system for the future aircraft design investigated in the German Collaborative Research Center 880 (SFB880 for “Sonderforschungsbereich 880” in German). [1] The motivation for the research in this project stems from the need to improve aircraft flying efficiency, generate large lift coefficients with low noise thereby enabling operations from smaller less congested airports closer to neighborhoods and thus reducing door-to-door travel times, and to allow flexibility to changes in the design over the aircraft lifetime. With such enhancements to aircraft, growth of the industry can be ensured in a sustainable manner. A number of technologies, including the droop-nose device, are being investigated in the project and for more information the reader is referred to Refs. [1–3]. The droop-nose device under research is gapless and therefore quieter than current slats, and smoothly varying thereby ensuring a good pressure gradient delaying stall and reducing the demand on the internal compressor system. With such qualities the droop-nose device is a

mandatory component of this new high-lift system. Further advantages could include increased laminarity due to the droop-nose being stepless.

The design of the droop-nose device is largely driven through structural optimization tools given the large number of design variables and whose optima are non-intuitive. The development of the tools and the design itself follows on from previous works. Kintscher et al. [4] developed a fiberglass droop-nose device in the SADE project which was manufactured at 1:1 scale and wind tunnel tested, and Kintscher et al. [5] in a separate project (SARISTU) considered aspects of anti/de-icing, lightning protection, erosion, and bird-strikes in the droop-nose design. Rudenko et al. [6] developed a 2D section of a droop-nose demonstrator composed of a hybrid fiberglass-elastomer material to enable large deflections also as part of the SFB880 project [7]. Vasista et al. manufactured and wind tunnel tested a 3D droop-nose for a wingtip featuring a flexible skin and superelastic compliant mechanism as part of the NOVEMOR project [8–10]. Radestock et al. [11] manufactured a droop-nose for a UAV which was flight tested as part of the CHANGE project. Other works on morphing droop-nose devices can be found in Refs. [12–14].

This paper presents the design of the droop-nose device as it nears completion and the manufacturing stage. The aircraft geometry, and aerodynamic and spar bending loads is first presented, followed by intermediate results of the design. A discussion on the design and roadmap to manufacture are subsequently presented.

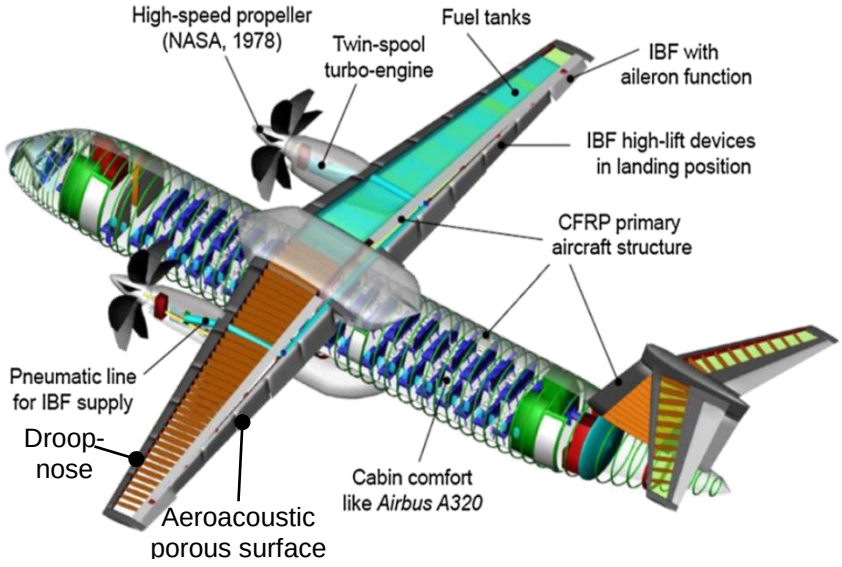

Figure 1 One of the reference aircraft configurations investigated in the SFB880 project.

2 DESIGN CHAIN, GEOMETRY, AND LOADS

A high-wing turboprop aircraft considered as one of multiple reference configurations in the project is shown in Fig. 1 and is designed for a range of 2,100 km for a payload of 12,000 kg. The 2D geometry of the droop-nose in clean (cruise) and droop (approach) configurations is shown in Fig. 2a-c. The droop-nose requires a camber variation of 90° at the leading edge point and the magnitude of curvature change is shown in Fig. 2d, with a maximum value of

0.017 mm^{-1}. The overall process chain of the droop-nose design is presented in Fig. 3. Geometry and loading calculated by project partners is transferred to the skin optimization tool in which the skin thickness distribution and locations and magnitudes of forces acting on the stringer load introduction points are determined. The design of the internal kinematic mechanisms is subsequently performed and reintegrated with the skin finite element model. Upon a successful design, the droop-nose is then manufactured.

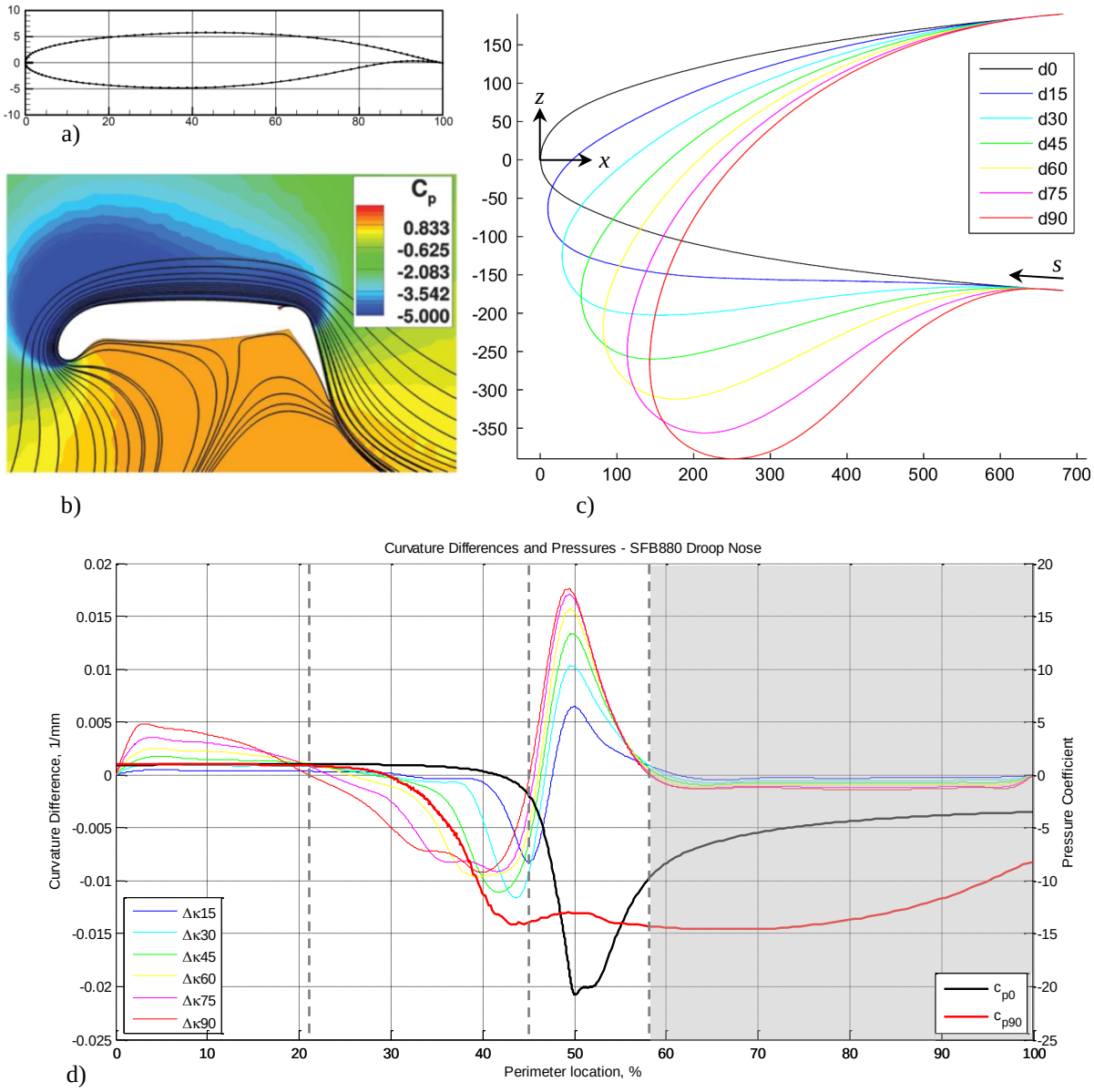

Figure 2. a) DLR F15 aerofoil. b) CFD result presented in Ref. [2]. c) Droop target deflections. d) Shape change and loading requirements along the 2D leading edge profile. The grey dashed lines and area where Δκ is zero or low and pressure is high show potential locations for stringers.

The starboard wing 3D geometry of the leading edge is shown in Fig. 4 and is segmented along the span. The droop-nose segments have been taken perpendicular to the front spar and normal to the dihedral angle to minimize stresses. A number of aerodynamic load cases at various angles of attack (AoA) and inertial load cases (calculated by project partners) have been considered in the design as shown in Table 1. A radial basis function (RBF) tool was used to transfer the pressures and bending on to the mesh for the droop-nose finite element analysis as shown in Fig. 5 as an example.

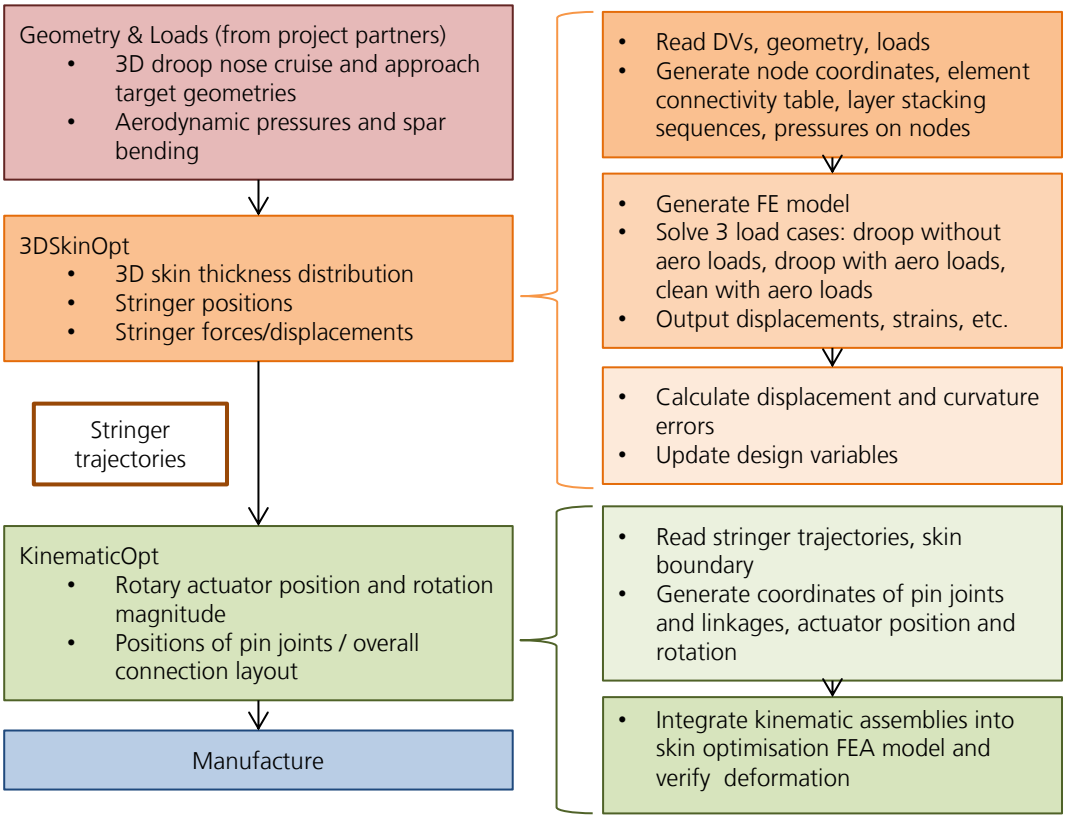

Figure 3 Design chain of the droop-nose device with supporting kinematic mechanisms.

Table 1. Summary of load cases considered.

Aerodynamic Pressures
cruise (clean shape) 3 deg. AoA
approach (droop shape) 0 deg. AoA
approach (droop shape) c_{Lmax}
Spar Bending
cruise (clean shape) 1 g
approach (droop shape) 1 g
landing (droop shape) 4 g
maneuver (clean shape) 2.5 g

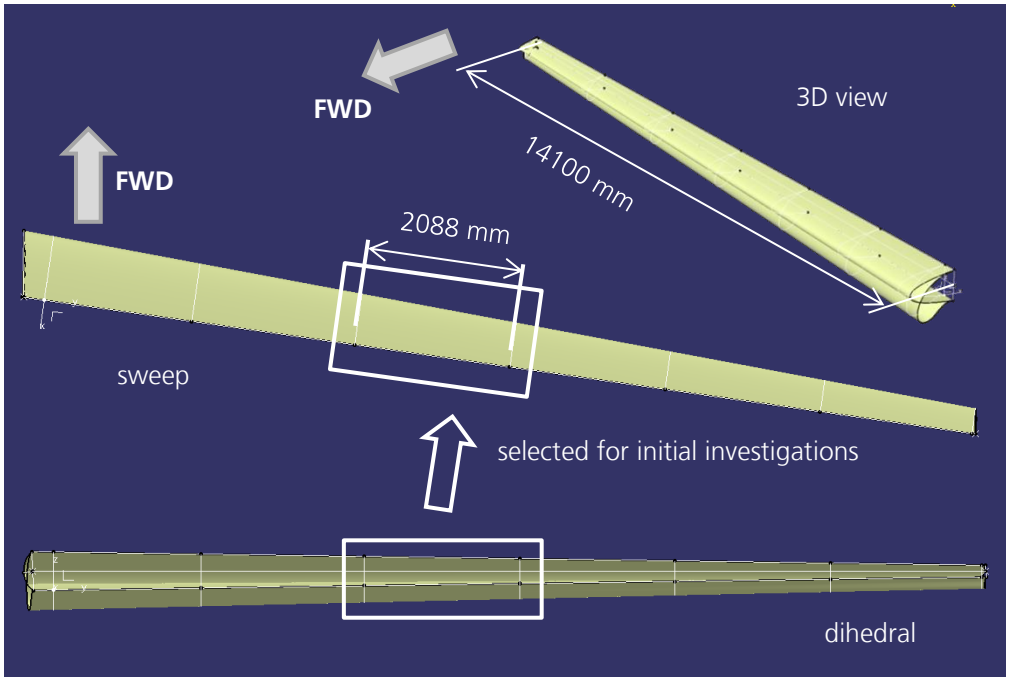

Figure 4 3D geometry of the droop-nose segments on the starboard wing.

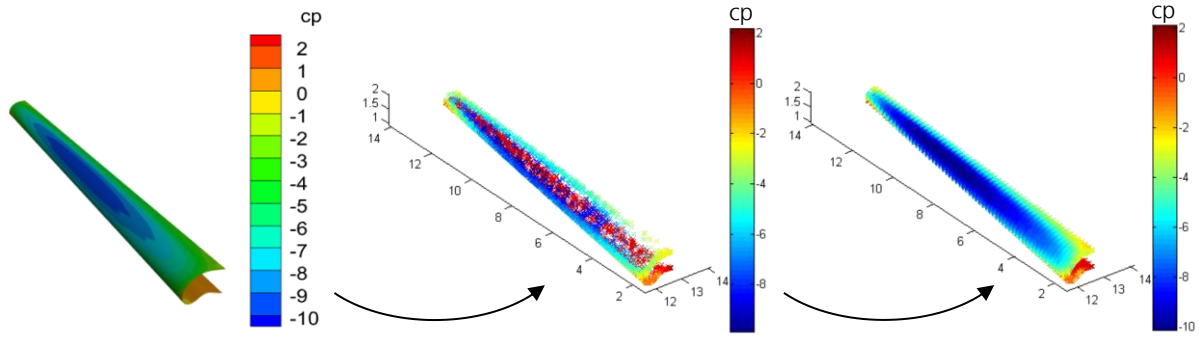

a) surface contour display of CFD results

b) point cloud display of CFD results

c) c_p values at FEA nodes

Figure 5 Example of mapping approach c_{Lmax} pressure loads from CFD to FEA meshes through a radial basis function tool.

3 SKIN DESIGN

The selected droop-nose segment is shown in Fig. 6 with clean and droop surfaces and is intended to be produced with a composite skin attached to kinematic mechanisms at three spanwise stations through stringers at various locations along the profile perimeter. The composite skin is composed of HexPly® 913 fiberglass prepreg layers in combination with ethylene propylene diene monomer (EPDM) elastomer as shown in Fig. 7 and was previously designed in this project. Stiffness can be tailored by determining the best thickness distribution of the material over the full surface and physically captured by dropping-off plies with corresponding geometries. More details on this hybrid material combination are provided

in Ref. [7] and such a hybrid lay-up was used to ensure sufficient stiffness in the spanwise direction and sufficient flexibility in the chordwise morphing direction. Material characterization was performed and orthotropic properties were generated from homogenization procedures. This material information was used in the finite element analysis subroutines where layered shell elements with multiple plies in orientations as specified by a plybook were used. The optimization procedure and the ensuing results are presented in this section.

3.1 3D Skin Optimization Method

The optimization method is based on that of Refs. [4,8] with modifications necessary for the large displacements and 3D analysis made in this work. The optimization solver is the Nelder - Mead Simplex local method [15] and is suited given the non-differentiable nature of this optimization problem. In total 24 design variables were used which included 14 skin thickness points (7 at the inboard and outboard aerofoil profiles and bilinearly interpolated between to map the thickness over the entire droop-nose surface), 5 stringer position points, and 5 force values (scaled along the span and applied at the 15 force application points i.e. 5 stringers × 3 ribs). It should be noted that modifications to the optimization tool included the ability to easily change mesh fidelity as the computation time is high, and easily change the number of stringers. The overall process is shown in Fig. 3. The objective function was to minimize the combined displacement and curvature error over the droop-nose surface over three different load cases, namely droop under actuation load without aerodynamic load, droop under actuation load with aerodynamic load, and clean under blocked actuator with aerodynamic load. Spar bending was omitted at this stage and is checked at the end of the optimization procedure.

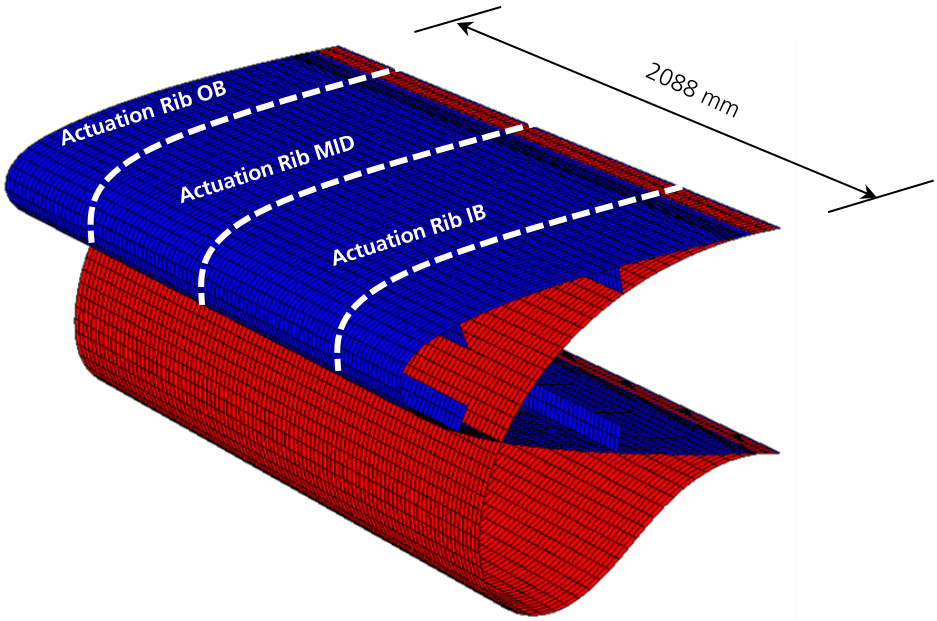

Figure 6 Concept of a single droop-nose segment showing kinematic rib stations.

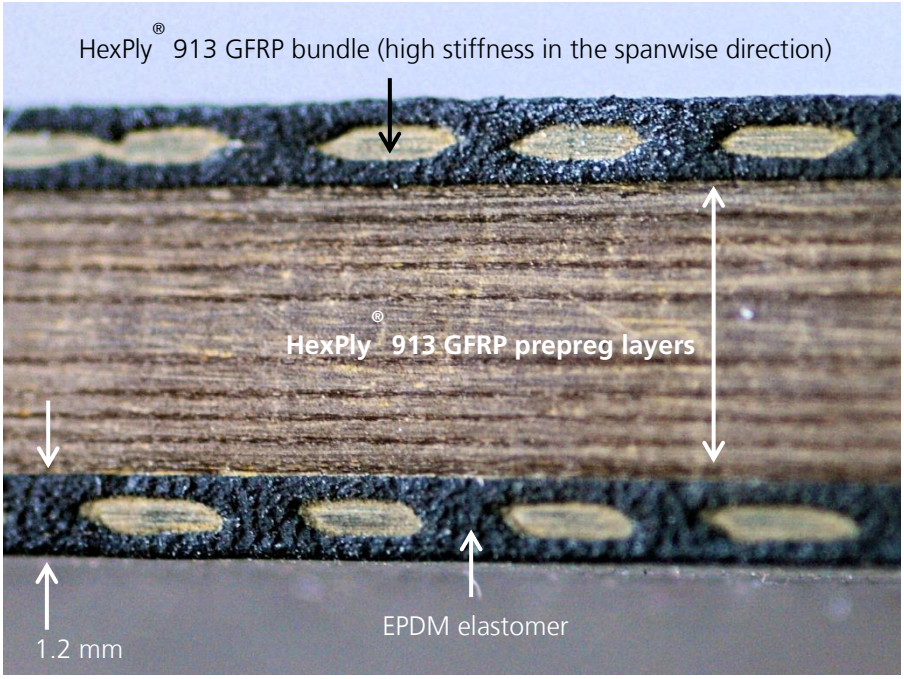

Figure 7 Cross-section view of the hybrid GFRP-EPDM composite skin

3.2 3D Skin Optimization Results

Displacement, curvature, strain and reaction forces output by the skin optimization tool are presented in this section. Fig. 8 shows the resultant profile shapes under the different load cases at the root and tip locations of the droop-nose segment. It is clear that the target shape is appropriately met under all load cases thus verifying the suitability of the optimization tool to find optimum values of the design variables. The mean curvature errors presented in Fig. 9a further confirms this with the errors being in the range of 1.5×10^{-3} mm^{-1}. The thickness distribution shown in Fig. 9b depicts higher thickness towards to the spar and root and lower thickness towards the leading edge and tip section. This is expected given the target curvature difference function shown in Fig. 2d and the taper in chord and profile height along the span. The strain results in Fig. 9c show that maximum strain occurs due to the straightening of the leading edge line from the clean configuration to droop configuration. The contours are shown for the outer EPDM layers and for the outermost GFRP layers the strain was in the order of 1.5%. The strains for the cruise configuration in Fig. 9d show low holding strains even in the outermost EPDM layers at 0.3%.

4 KINEMATIC MECHANISM DESIGN

It is envisaged that the skin is supported by a set of metallic mechanical linkages and pin joints connected to rotational actuators. The kinematic linkages need to move in the paths the stringers would assume as calculated in the skin optimization stage. An additional optimization tool has been used to determine the kinematic mechanism design.

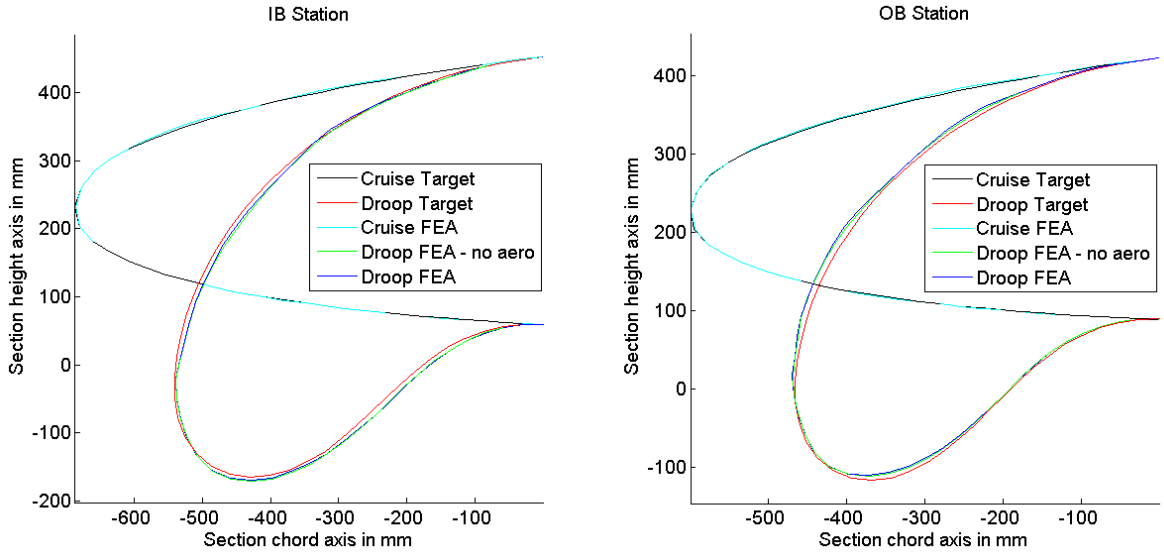

Figure 8 Root (IB) and tip (OB) profile shape results under different load cases.

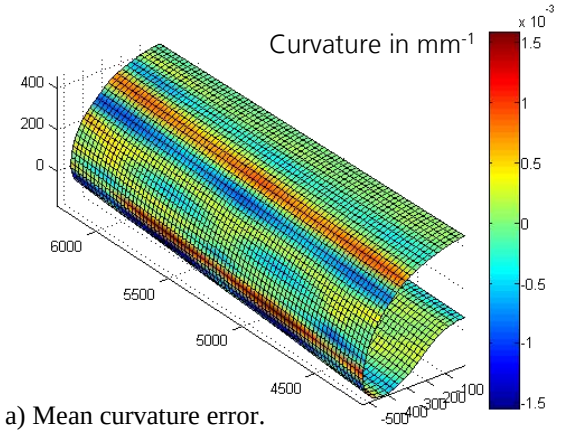

a) Mean curvature error.

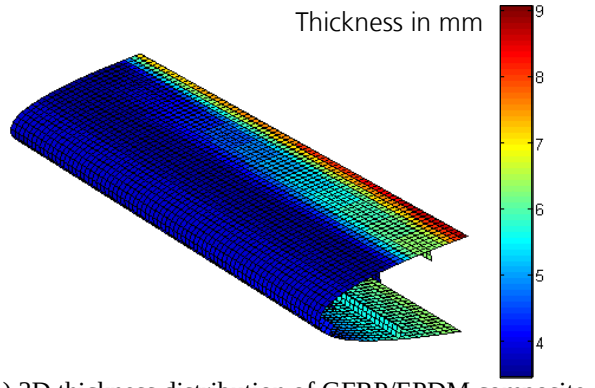

b) 3D thickness distribution of GFRP/EPDM composite.

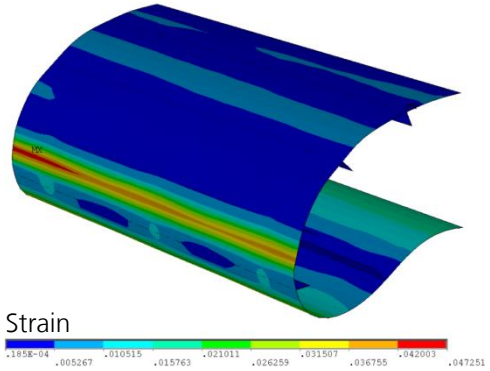

b) Outer layer strain results at approach $c_{L\max}$.

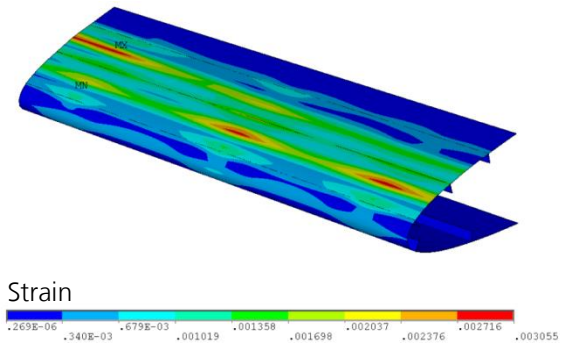

b) Outer layer strain results at cruise, 3 deg. AoA.

Figure 9 Results of the 3D skin optimization stage.

4.1 Kinematic Optimization Method

The kinematic optimization tool uses a local optimization solver to determine the locations of pin joints and linkage lengths. The tool cycles over the number of stringers and for each stringer a single joint in the connection between actuator and stringer is used. In this way, the path to each stringer is independently calculated though using the same actuator position and magnitude of rotation for all actuator-stringer paths. The design variables are the positions of the pin joints $P(x, z)$, the actuator position (x_d, z_d) and the actuator rotation angle ϕ as shown in Fig. 10. The objective function is to minimize the length error between the moving pin joint-target trajectory point $(L_i - L_1)$ over all m target trajectory points.

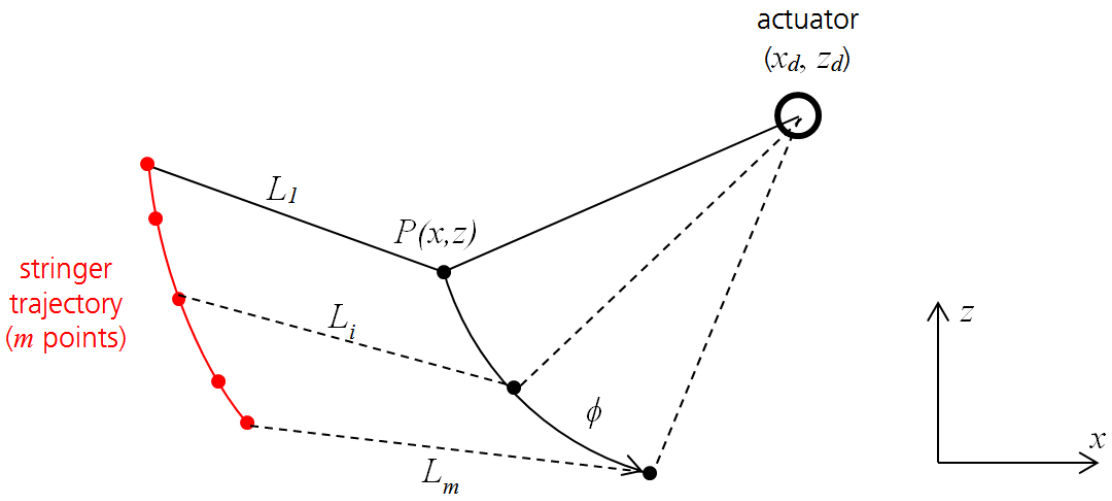

Figure 10 Kinematic mechanism optimization tool design variables.

4.2 Kinematic Optimization Results

The resultant inboard kinematic design is shown in Fig. 11a as an example. The mid span and outboard kinematic stations featured similar results. An example search history of the pin joint for stringer 2 is shown in Fig. 11b with dark red being the worst location and dark blue and the overlaid green cross being the best location of the pin joint. In this case the maximum length error over the trajectory points was 0.62 mm. One drawback of the method is that given the skin is flexible, the actual assumed point by the stringer may fall anywhere on the circle prescribed by the linkage from the pin joint to the stringer. This needs to be addressed in future work.

4.3 Integration into the Skin Model

The resulting kinematic linkages were input into the existing skin finite element model as multipoint constraint rigid link and spherical joint elements. The strain results in Fig. 12 and show that the deformation under actuation load and transmission through the kinematic linkages results in appropriate droop deformation. The strain values remain in the order of 1.5% for the outermost GFRP layers and the actuator torque for the different load cases are shown in Table 2. It can be seen that actuator torque requirements are relatively high with

maximum values of 1765, 3587 and 527 Nm for the cases of droop without aerodynamic loads, droop with maximum approach loads, and clean with cruise aerodynamic loads respectively. From the difference with and without approach loads, it can be seen that the external pressure loading itself requires approximately 2000 Nm of torque. Whilst these values are high, they are producible through actuators such as harmonic drives or traditional torque tube and reduction gearbox transmission systems as used in conventional aircraft. Reduction in actuator torque could be possible by positioning the actuator closer to the foremost stringers thereby reducing the moment arm and thus torque.

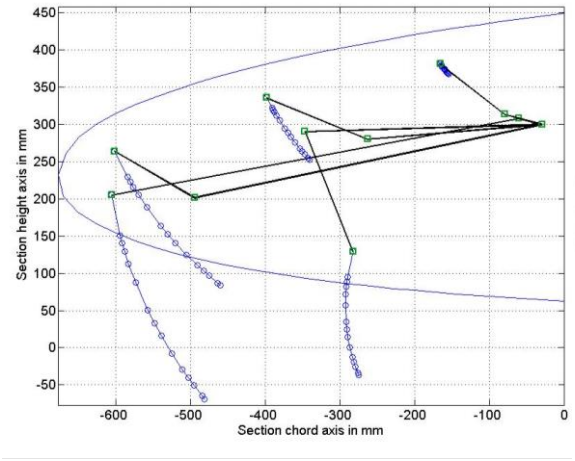

a) Kinematic design of the inboard station.

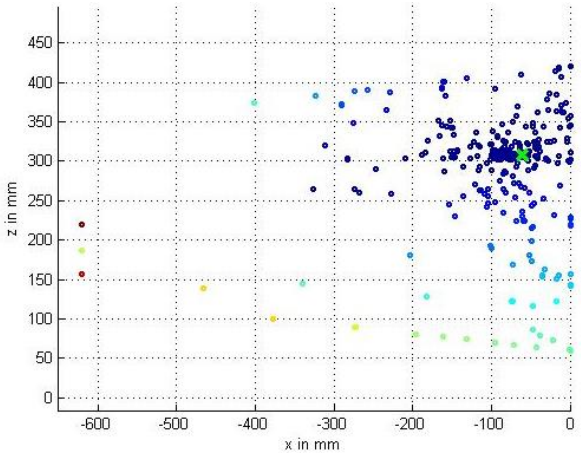

b) Sampled search points with length error for stringer 2. Red points have large errors and blue points have low. The green cross is the best found location.

Figure 11 Results of the kinematic optimization stage.

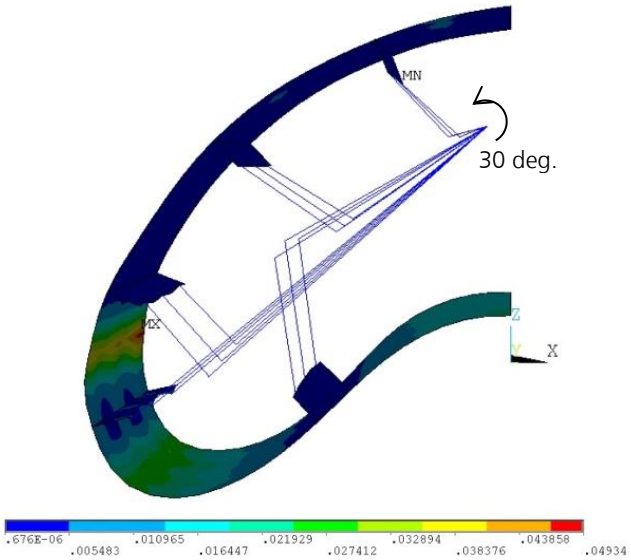

Figure 12 Finite element strain results at outer EPDM layers with kinematic linkages and actuator rotation.

Table 2 Actuator rotation and torque results.

Station	Rotation, deg.	Torque, N·m
Droop, no aeroload		
IB	30	910
MID	30	1765
OB	30	1323
Droop, $c_{L\max}$ approach		
IB	30	2782
MID	30	3587
OB	30	2535
Clean, 3 deg. AoA cruise		
IB	0	527
MID	0	431
OB	0	164

5 CONCLUSIONS AND FUTURE WORK

The procedure of the structural design of a large displacement morphing wing leading edge was presented in this work and intermediary results show the validity of the methods used. A number of tasks are required to refine the design before the manufacture stage, namely the post-optimization validation with bending loads applied, the inclusion of draping effects along the 3D surface and orientation of the stackings of individual elements, the improvement of the kinematic optimization procedure to ensure kinematic trajectories match the targets, and the inclusion of strap material for the connection of the linkages to the stringers as this will be necessary in the manufactured part. Parallel to this design, the design of compliant substructures is also being investigated for comparison purposes.

ACKNOWLEDGMENTS

The authors are grateful for the financial support from the German Research Foundation (Deutsche Forschungsgemeinschaft DFG) for funding as part of the Collaborative Research Center 880 (Sonderforschungsbereich SFB880).

REFERENCES

[1] Radespiel, R., and Heinze, W., "SFB 880: Fundamentals of High Lift for Future Commercial Aircraft," *CEAS Aeronautical Journal*, Vol. 5, No. 3, 2014, pp. 239–251, DOI: 10.1007/s13272-014-0103-6.

[2] Burnazzi, M., and Radespiel, R., "Design and Analysis of a Droop Nose for Coanda Flap Applications," *Journal of Aircraft*, Vol. 51, No. 5, 2014, pp. 1567–1579, DOI: 10.2514/1.C032434.

[3] Seume, J., Teichel, S., Burnazzi, M., Schwerter, M., Behr, C., Rudenko, A., Schmitz, A., Dörbaum M., and Atalayer, C., "SFB 880 - Efficient High Lift," *Deutscher Luft- und Ramfahrtkongress*, 2013.

[4] Kintscher, M., Wiedemann, M., Monner, H. P., Heintze, O., and Kühn, T., "Design of a

Smart Leading Edge Device for Low Speed Wind Tunnel Tests in the European Project SADE," *International Journal of Structural Integrity*, Vol. 2, No. 4, 2011, pp. 383–405, DOI: 10.1108/17579861111183911.

[5] Kintscher, M., Kirn, J., Storm, S., and Peter, F., "Assessment of the SARISTU Enhanced Adaptive Droop Nose," *Smart Intelligent Aircraft Structures (SARISTU): Proceedings of the Final Project Conference*, P.C. Wölcken and M. Papadopoulos, eds., Springer International Publishing, Switzerland, 2016, pp. 113–140, DOI: 10.1007/978-3-319-22413-8_6.

[6] Rudenko, A., Monner, H. P., and Rose, M., "A Process Chain for Structural Optimization of a Smart Droop Nose for an Active Blown High Lift System," *22nd AIAA/ASME/AHS Adaptive Structures Conference (SciTech 2014)*, January 13-17, AIAA Paper 2014-1414, National Harbor, Maryland, 2014, DOI: 10.2514/6.2014-1414.

[7] Schmitz, A., and Horst, P., "A New Curvature Morphing Skin: Manufacturing, Experimental and Numerical Investigations," *European Conference on Composite Materials*, 22-26 June 2014, Seville, Spain, 2014.

[8] Vasista, S., De Gaspari, A., Ricci, S., Riemenschneider, J., Monner, H. P., and van de Kamp, B., "Compliant Structures-Based Wing and Wingtip Morphing Devices," *Aircraft Engineering and Aerospace Technology*, Vol. 88, No. 2, 2016, DOI: 10.1108/AEAT-02-2015-0067.

[9] Vasista, S., Riemenschneider, J., van de Kamp, B., Monner, H. P., Cheung, R. C. M., Wales, C., and Cooper, J., "Lessons Learned from Wind Tunnel Testing of a Droop-Nose Morphing Wingtip," *SPIE Proceedings Active and Passive Smart Structures and Integrated Systems 2016*, Vol. 9799, 2016, pp. 1–9, DOI: 10.1117/12.2219163.

[10] Vasista, S., Riemenschneider, J., van de Kamp, B., Monner, H. P., Cheung, R. C. M., Wales, C., and Cooper, J. E., "Evaluation of a Compliant Mechanism-Based Droop-Nose Morphing Wingtip via Experimental Tests," *Journal of Aircraft*, 2017.

[11] Radestock, M., Riemenschneider, J., Monner, H. P., and Rose, M., "Structural Optimization of an UAV Leading Edge with Topology Optimization," *DeMEASS*, 2014.

[12] De Gaspari, A., and Ricci, S., "A Two-Level Approach for the Optimal Design of Morphing Wings Based On Compliant Structures," *Journal of Intelligent Material Systems and Structures*, Vol. 22, No. 10, 2011, pp. 1091–1111, DOI: 10.1177/1045389X11409081.

[13] Sodja, J., Martinez, M. J., Simpson, J. C., and De Breuker, R., "Experimental Evaluation of the Morphing Leading Edge Concept," *23rd AIAA/AHS Adaptive Structures Conference (SciTech 2014)*, January 5-9, AIAA Paper 2015-0791, 2015, DOI: 10.2514/6.2015-0791.

[14] Weber, D., Mueller-Roemer, J. S., Simpson, J. C., Adachi, S., Herget, W., Landersheim, V., and Laveuve, D., "Smart Droop Nose for Application to Laminar Wing of Future Green Regional A/C," *Greener Aviation*, Brussels, Belgium, 2014.

[15] Lagarias, J. C., Reeds, J. A., Wright, M. H., and Wright, P. E., "Convergence Properties of the Nelder--Mead Simplex Method in Low Dimensions," *SIAM Journal on Optimization*, Vol. 9, No. 1, 1998, pp. 112–147, DOI: 10.1137/S1052623496303470.